Opportunities for production and property research of neutron-rich nuclei around N=126 at HIAF

Shao-Bo Ma,[1,2] Li-Na Sheng,[1,3] Xue-Heng Zhang,[1,2,3,*] Shi-Tao Wang,[1,3] Kai-Long Wang,[1,3] Chun-Wang Ma,[4,5] Hool-Jin Ong,[1,3,6,7,8] Zhi-Yu Sun,[1,2,3] Shu-Wen Tang,[1,3] Yu-Hong Yu,[1,2,3] Xin-Tong Du,[1,9] and Xiao-Bao Wei[1,4]

[1]*Institute of Modern Physics, Chinese Academy of Sciences, Lanzhou 730000, China*
[2]*Advanced Energy Science and Technology Guangdong Laboratory, Huizhou, 516000, China*
[3]*University of Chinese Academy of Sciences, Beijing 100049, China*
[4]*College of Physics, Henan Normal University, Xinxiang 453007 China*
[5]*Institute of Nuclear Science and Technology, Henan Academy of Science, Zhengzhou 450046, China*
[6]*Joint-Department for Nuclear Physics, Lanzhou University and Institute of Modern Physics, Lanzhou 730000, China*
[7]*Research Center for Nuclear Physics, Osaka University, Osaka 567-0047, Japan*
[8]*RIKEN Nishina Center, Saitama 351-0198, Japan*
[9]*Northwest Normal University, Lanzhou 730070, China*

The study of nuclide production and its properties in the N=126 neutron-rich region is the frontier and hot topic in nuclear physics and astrophysics research. The upcoming High energy FRagment Separator (HFRS) at the High Intensity heavy-ion Accelerator Facility (HIAF), an in-flight separator at relativistic energies, is characterized by high beam intensity, large ion-optical acceptance, high magnetic rigidity, and high momentum resolution power. It provides an opportunity for the study of the production and properties of neutron-rich nuclei around N=126. In this paper, an experimental scheme is proposed to produce the neutron-rich nuclei around N=126 and simultaneously measure their mass and lifetime based on the HFRS separator, and the feasibility of this scheme is evaluated by the simulations. The results show that under the high resolution optical mode many new neutron-rich nuclei approaching the r-process abundance peak around A=195 can be produced for the first time, and many nuclei with unknown mass and lifetime can be produced with high statistics. Using the time-of-flight corrected by the measured dispersive position and the energy loss information, the cocktails produced from the ^{208}Pb fragmentation can be unambiguously identified. Moreover, the masses of some neutron-rich nuclei in the vicinity of N=126 can be measured with high precision using the time-of-flight magnetic rigidity technique. This indicates that the HIAF-HFRS facility has potential for the production and property research of neutron-rich nuclei around N=126, which is of great significance for expanding chart of nuclides, developing nuclear theories, and understanding the origin of heavy elements in the universe.

Keywords: HFRS, fragmentation, neutron-rich nuclei around N=126, mass measurement, lifetime

I. INTRODUCTION

The study of nuclide production and its properties in the N=126 neutron-rich region is of great significance to expand the nuclear landscape, revealing the evolution of shell structure, and understand the astrophysical nucleosynthesis. According to the theory of nuclear astrophysics, approximately half of the nuclei in nature heavier than iron are considered to be produced by the rapid neutron capture process, also known as the r-process [1–3]. The properties of N=126 neutron-rich nuclei, such as mass and lifetime, play a crucial role in understanding the r-process abundance peak around A=195 [4–6]. However, reaching this region experimentally is difficult because of the low production cross-sections and the great challenge of separation and identification. The lack of experimental data leads to significant uncertainty in the predicted abundance patterns [7–10]. Therefore, the production and property research of neutron-rich nuclei around N=126 is of exceptional importance.

In the last decades, the production of N=126 neutron-rich nuclei in the laboratory has been a challenging problem. Multi-nucleon transfer (MNT) reactions at near-barrier energies are expected to be a powerful technique for the synthesis and study of nuclides in the neutron-rich N=126 region [11–14]. Several facilities based on MNT reactions have been constructed or are in planning or under construction around the world, such as KISS at RIKEN [15], IGISOL at JYFL [16], the N=126 factory at ANL [17], and INCREASE at GSI [18]. Some neutron-rich isotopes of Pt, Ir, and Os, which were produced as target-like fragments using the ^{136}Xe+^{198}Pt reaction system, have been successfully extracted using the KISS facility [19, 20]. However, to reduce the plasma density in the gas cell induced by the primary beam and elastic products [15, 21, 22], the experiments using these facilities are usually carried out at low primary beam intensities. Moreover, thin reaction targets must be used due to the low beam energy in the experiments. Low beam intensity and thin reaction targets are not beneficial for obtaining high fragment yields. To increase the available primary beam intensity, a new design using a gas-filled solenoid to suppress unwanted elastic particles has been proposed in future facilities such as NEXT at Groningen [23] and KISS-II at RIKEN [24].

Except for the MNT reactions at near-barrier energies, the experimental results indicate that the projectile fragmentation reaction of ^{208}Pb or ^{238}U at relativistic energies may be an effective method for producing heavy neutron-rich nuclei in this region [25, 26]. But this method requires conditions of high beam intensity, relativistic beam energy, and high performance of in-flight separator to be met simultaneously. High beam intensity is a necessary conduction for

* Corresponding author, zhxh@impcas.ac.cn

producing low cross-section products. Relativistic energy is required to reduce the number of populated ionic charge states, thereby increasing the collection efficiency. High performance separators are crucial for the separation and identification of heavy neutron-rich fragments [27]. The future Super-FRS in-flight facility at FAIR [28] meets these conditions. Searching new isotopes and studying their properties in the region along the N=126 line below ^{208}Pb have been proposed as one of the main physical objectives during FAIR Phase-0 experiments [29].

High energy FRagment Separator (HFRS) [30, 31], an in-flight separator at relativistic energies, is now under construction at the High Intensity heavy-ion Accelerator Facility (HIAF) [32, 33] and will start operation a few years from now. It is also characterized by large ion-optical acceptance, high resolution power, high magnetic rigidity, and excellent particle identification, just like the Super-FRS separator. In combination with the HIAF accelerator facility, which will provide beams up to $34\,\mathrm{Tm}$ corresponding to ^{238}U^{35+} ions of $833\,\mathrm{MeV/nucleon}$ and with an intensity as high as 1×10^{11} ions per pulse, the neutron-rich nuclei around N=126 from projectile fragmentation at relativistic energies can be produced and purified by using the HFRS separator. This provides a new opportunity for studying the properties of N=126 neutron-rich nuclei and understanding the third abundance peak in the r-process.

In this paper, we mainly concentrate on the production of N=126 neutron-rich nuclei and the feasibility of studying their properties using the HIAF-HFRS facility. The measurement methods for nuclear properties such as mass and lifetime, as well as the layout of related experimental setups, will be introduced first. Then the simulation results will be presented to check the feasibility.

II. EXPERIMENTAL SETUPS AND METHODS

Nuclear masses and lifetimes are of fundamental importance for r-process simulations. Using the HFRS separator at the HIAF facility, some neutron-rich nuclei in the region along the N=126 line below ^{208}Pb could be produced, and the properties of these nuclei, such as mass and lifetime, could be experimentally measured.

The layout of experimental setups of the HFRS separator is shown in Fig. 1. A relativistic ^{208}Pb or ^{238}U primary beam will be extracted from the HIAF accelerator facility in a slow extraction mode and implanted into the carbon production target at the entrance of the HFRS separator. The fragments of interest produced via the fragmentation reaction will be collected and separated using the $B\rho$-ΔE-$B\rho$ method [34, 35], in which the analysis of the magnetic rigidity ($B\rho$) is combined with the energy loss in an achromatic degrader (ΔE) at the pre-separator stage. The achromatic degrader will be placed at the PF2 dispersive plane. The unreacted primary beam will be intercepted in the beam dump systems installed after each dipole magnet in the pre-separator according to $B\rho$ deviation between the primary beam and the desired isotope.

The main-separator will be used as a spectrometer. At this stage, the cocktail products will be identified by combining the ΔE-TOF-$B\rho$ method and the isomer tagging technique [36–38]. The energy loss (ΔE), time of flight (TOF), and the $B\rho$ are measured and used to determine the atomic number Z and the mass-to-charge ratio A/Q of the fragments. By detecting delayed γ-rays emitted from short-lived isomeric states of certain fragment, the cocktails can be unambiguously identified. The schematic layout of the particle identification setups can be seen in Fig. 1. A multiple sampling ionization chambers (MUSIC) placed at the MF6 will be used for the ΔE measurement [39, 40]. The TOF information will be obtained from the TOF detectors installed at the PF4 and MF6 foci with a flight path of $118.03\,\mathrm{m}$ [31, 41]. The $B\rho$ value will be determined from the position measurements at the MF4 dispersive plane. At the final focal plane of the HFRS a decay detector array, which is consists of a silicon array stopper and surrounded by an array of high-purity germanium detectors, will be used for the isomer tagging of the selected fragments.

In the ΔE-TOF-$B\rho$ method, the mass-to-charge ratio A/Q of a fragment is determined using the equations as follows:

$$TOF = \frac{L}{v}, \tag{1}$$

$$\frac{A}{Q} = \frac{B\rho}{\gamma v}. \tag{2}$$

Here L is the length of flight path, v is the velocity of the fragment, and γ is the relativistic Lorentz factor. The fragment mass m can then be expressed as,

$$m = Q\frac{B\rho}{c}\sqrt{(\frac{cTOF}{L})^2 - 1}, \tag{3}$$

where c represents the velocity of the light. From this equation, the nuclear mass can be measured from the measured TOF and $B\rho$ while performing particle identification. This nuclear mass measurement method is called the $B\rho$-TOF method [42, 43]. Usually, the precise $B\rho$ determination is achieved by the trajectory reconstruction method [44]. Assuming negligible the object spot size, the $B\rho$ values can be calculated simply from the following formula,

$$B\rho = B\rho_0[1 + \frac{x_D}{(x|\delta)}], \tag{4}$$

here $B\rho_0$ represents the central magnetic rigidity. The x_D and $(x|\delta)$ denote the horizontal position and the momentum dispersion at the dispersive plane, respectively. The $B\rho$-TOF method has the characteristics of simple equipment, high measurement accuracy, low requirement for fragment yield, and short measurement time, making it particularly suitable for measuring the mass of short-lived nuclei with very low yield far from the stability line. Using this method, the masses of some very neutron-rich nuclei have been accurately measured for the first time, such as the masses of ^{48,49}Ar and ^{56,57}Sc measured with the combination of the A1900 separator and S800 spectrometer at NSCL [45, 46], the masses of

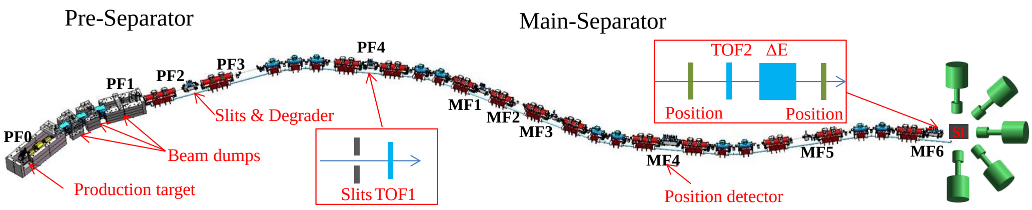

Fig. 1. (Color online) Schematic layout of experimental setups of the HFRS separator.

$^{55-57}$Ca, $^{58-60}$Sc, $^{60-62}$Ti, and $^{62-64}$V measured with the combination of the BigRIPS separator and the SHARAQ spectrometer at RIKEN [47, 48].

From Eqs. (3) and (4), the mass resolution σ_m/m of the $B\rho$-TOF method can be deduced as,

$$\begin{aligned}(\frac{\sigma_m}{m})^2 &= (\frac{\sigma_{B\rho}}{B\rho})^2 + (\frac{\gamma^2\sigma_{TOF}}{TOF})^2 \\ &= (\frac{\sigma_{x_D}}{(x|\delta)+x_D})^2 + (\frac{\gamma^2\sigma_{TOF}}{TOF})^2,\end{aligned} \tag{5}$$

where σ_i is the standard deviation of measured values of "i". To improve the mass measurement accuracy, the common method is to simultaneously improve the position resolution of the position detector placed at the dispersive plane, the time resolution of the TOF system, and the momentum dispersion. For position measurement at the dispersion focal plane, detectors with thin material thickness should be used to reduce the impact of beam energy loss and multiple scattering on the beam trajectory. A position-sensitive micro-channel-plate (MCP) tracking detector with a resolution of $\sim$0.5 mm (σ) [49] and a low-pressure delay-line parallel-plate avalanche counter (DL-PPAC) with a resolution of $\sim$0.43 mm (σ) [50] were used for the $B\rho$-TOF mass measurement experiments at NSCL and RIKEN, respectively. Using a typical resolution of $\sim$0.5 mm (σ) of the position detector at the dispersive plane, combined with a high-resolution optical mode with a momentum dispersion of $\sim$10 cm/% specially designed for the HFRS main separator, the uncertainty $\sigma_{B\rho}/B\rho$ can be estimated to be about 5×10^{-5}

For the TOF measurement, the lower the ion energy, the longer its flight time, which is more conducive to improving TOF measurement accuracy. However, for N=126 neutron-rich heavy nuclei, low ion energy can cause changes in the charge state population passing through the materials placed at the foci, thereby affecting collection efficiency. Fig. 2 (a) shows the fractions of fully stripped ions in the equilibrium charge state after passing through an Al degrader for the elements in the N=126 region as a function of the kinetic energy behind the degrader. It was calculated with the Global code [51]. One can observe that the fractions of fully stripped ions decrease with increasing charge number and decreasing kinetic energy. When the ion energy behind the Al degrader is greater than 350 MeV/nucleon, even for the heaviest Hg element, the proportion of fully stripped ions is higher than 50 %. This proportion is acceptable for the mass measurement experiments. The flight path length of the HFRS is 118.03 m. Fig. 2 (b) shows the effect of the time resolution of the TOF system on mass measurement accuracy under different ion energies. For an ion with a kinetic energy of 350 MeV/nucleon, the contribution of TOF resolution to the final mass resolution is $\sim9.9\times10^{-5}$ under a system resolution of $\sim$30 ps (σ). This TOF resolution requirement can be achieved experimentally. For example, at NSCL, two plastic scintillator detectors readout by photomultiplier tubes were used for the TOF measurement, and the resolution was measured to be $\sim$30 ps (σ) with primary beam tests [52]. An upgraded TOF system for $B\rho$-TOF mass measurement experiments has been developed at the NSCL and achieved a better time resolution (σ) of 7.5 ps [53]. In addition, two CVD diamond detectors formed a TOF system used in RIKEN mass measurement experiments, with a system resolution of 27 ps (σ) [54].

Based on the contributions of position measurement accuracy ($\sim9.9\times10^{-5}$) and TOF measurement accuracy ($\sim5\times10^{-5}$) obtained above, a mass resolution of $\sim1.1\times10^{-4}$ can be obtained from the Eq. (5), which corresponds to σ_m $\sim$460 keV for $\sim$2000 statistics events and neutron-rich nuclei with mass number $\sim$200 near N=126. This accuracy of the mass excess is generally sufficient to reveal the evolution of shell structure and constrain mass models far from the stability [55].

Additionally, the mass shifts contributed by isomers will be estimated from the isomer measurement using the decay detector array at the final focal plane of the HFRS. The fragments will be stopped in the silicon array stopper after the mass measurement and the germanium detectors installed close to the stopper will be used to detect the isomeric γ-rays. From the measurement of the time elapsed between the implantation and the subsequent decay, the isomeric lifetime of the implanted ion can be obtained by correlating the particle identification of the HFRS. Simultaneously, using the stopper composed of multiple highly-pixelated Double-Sided Silicon Strip Detectors (DSSDs) such as AIDA [56] or WAS3ABi [57], the implanted nuclei and decay emitting β-rays can be directly correlated within each pixel of the detector, providing a direct measurement of the β-decay lifetimes. This is critical to our understanding of the third abundance peak in the r-process.

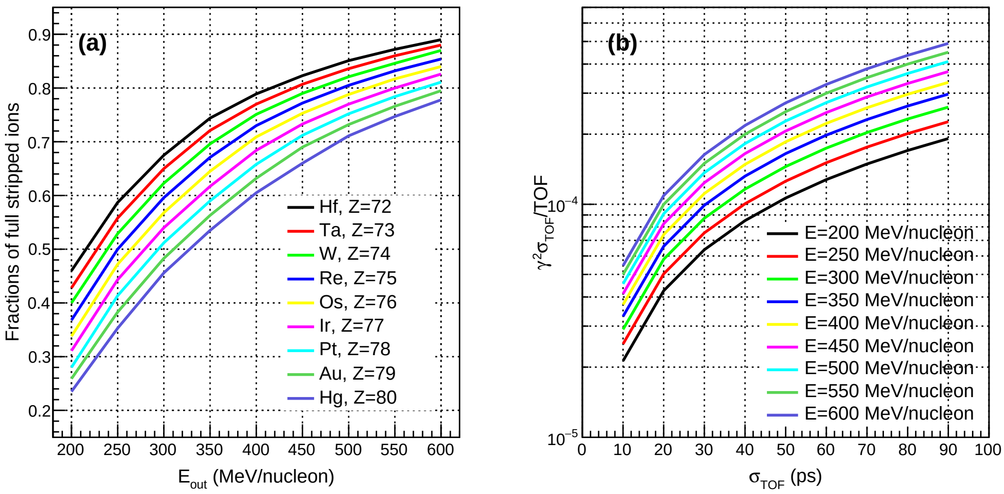

Fig. 2. (Color online) (a) Fractions of fully stripped ions in the equilibrium charge state after passing through an Al degrader for the elements in the N=126 region calculated with the Global code. (b) The effect of the time resolution of the TOF system on mass measurement accuracy under different ion energies.

III. SIMULATION AND ANALYSIS

With the HFRS separator at the HIAF facility, many neutron-rich nuclei around N=126 could be produced, and their properties, such as mass and lifetime, could be experimentally measured. This is of great significance for expanding nuclide maps, developing nuclear theories, and understanding the origin of heavy elements in the universe. In this section, we will first introduce a high resolution optical mode of the HFRS specifically developed for $B\rho$-TOF mass measurement experiments. Then the production, separation, identification, and nuclear mass measurement accuracy will be studied with the Monte Carlo simulation program MOCADI [58] using the high resolution ion-optics for the neutron-rich nuclei around N=126.

A. High resolution ion-optics

For $B\rho$-TOF mass measurement experiments, the pre-separator of the HFRS will be operated as a separator, and the main-separator will be used as a spectrometer. A high resolution ion-optics of the spectrometer is necessary in order to accurately measure ion magnetic rigidities. Using the parameterized magnetic field distributions [31], the high resolution ion-optics is designed with the codes of Winagile [59] and GI-COSY [60]. Fig. 3 shows the beam envelops with the initial beam spot sizes of X=$\pm 1\,\mathrm{mm}$ and Y=$\pm 1.5\,\mathrm{mm}$. To improve the momentum resolution, compared to normal mode [31], the horizontal angular acceptance is decreased to $\pm 5\,\mathrm{mrad}$ and the momentum acceptance is reduced to $\pm 0.2\,\%$. The maximum magnetic rigidity is also decreased from $25\,\mathrm{Tm}$ to $15\,\mathrm{Tm}$. The vertical angular acceptance remains unchanged at $25\,\mathrm{mrad}$. The momentum resolving power at the PF2 and MF4 is 1270 and 7440 , respectively, for an emittance of $5\,\pi$ mm mrad and a horizontal beam spot size of $\pm 1\,\mathrm{mm}$. The momentum dispersion at the MF4 is $12\,\mathrm{cm}/\%$. With this dispersion, the uncertainty of the $\sigma_{B\rho}/B\rho$ can be estimated to be about $\sim 4.17\times 10^{-5}$ using a typical resolution of $\sim 0.5\,\mathrm{mm}$ (σ) of the position detector at the dispersive plane.

B. Production and separation

To produce neutron-rich nuclei around N=126 by fragmentation reaction, the available projectiles mainly include ^{208}Pb and ^{238}U. In this simulation, both projectiles will be used. For a specific nucleus of interest, whether to use Pb fragmentation or U fragmentation will be determined based on the calculated yields. The Booster Ring (BRing) synchrotron of the HIAF facility has a maximum magnetic rigidity of $34\,\mathrm{Tm}$ and can accelerate $^{208}\mathrm{Pb}^{31+}$ and $^{238}\mathrm{U}^{35+}$ ions up to 850.74 and $833.15\,\mathrm{MeV/nucleon}$, respectively. The beam intensities of lead and uranium are as high as 1.1×10^{11} and 1.0×10^{11} ions per pulse, respectively. The typical beam extraction time in the slow extraction mode is $3\,\mathrm{s}$ with a repetition period of $13\,\mathrm{s}$. The corresponding beam spot in the X and Y directions on the production target are assumed to be of Gaussian distributions with standard deviations of $0.4\,\mathrm{mm}$ and $0.6\,\mathrm{mm}$, respectively.

Taking the production of ^{204}Au ions as an example, the production and separation ability for the neutron-rich nuclei around N=126 will be simulated and studied using the high resolution ion-optics of the HFRS. In the simulation, a graphite target installed at the PF0 focal plane will be used as the production target. The thickness of the graphite target will be set to $4.4\,\mathrm{g/cm^2}$ for both Pb and U fragmentation reactions, which corresponds to $50.1\,\%$ of the Pb range and

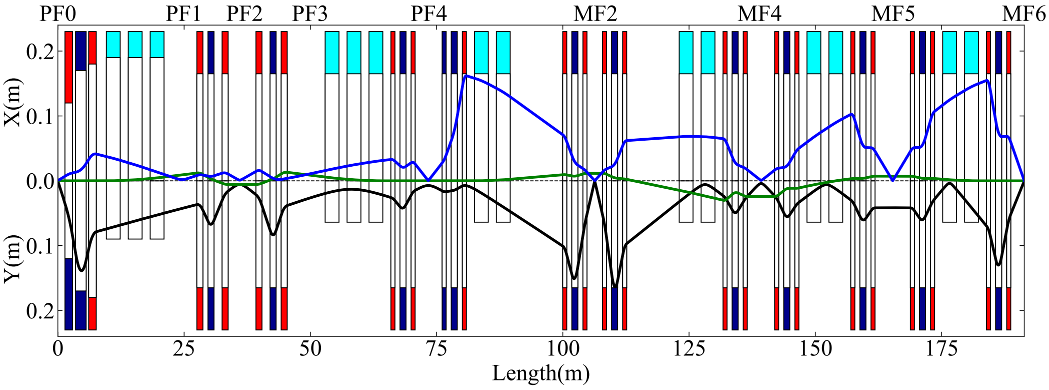

Fig. 3. (Color online) Beam envelopes for high resolution ion-optics. The blue line and the black line correspond to an emittance in the X-direction and Y-direction of $5\,\pi$ and $37.5\,\pi$ mm mrad, with an object size of $\pm 1\,\mathrm{mm}$ and $\pm 1.5\,\mathrm{mm}$ at the PF0, respectively, while the dispersion line (green) represents a momentum deviation of $+0.2\,\%$.

$56.5\,\%$ of the U range, respectively. In addition, a $75\,\mathrm{mg/cm^2}$ niobium foil is placed behind the production target to achieve efficient electron stripping in both reactions. More than $75\,\%$ of the ^{204}Au ions will be fully stripped, which is important for high transmission.

To purify the fragments of interest, an achromatic Al degrader placed at the PF2 dispersive plane will be used. As mentioned above, when the ion energy behind the Al degrader is greater than $350\,\mathrm{MeV/nucleon}$, the fraction of fully stripped ions is higher than $50\,\%$ for the neutron-rich nuclei around N=126. So the thickness of the degrader will be optimized to make the energy of fragments of interest greater than $350\,\mathrm{MeV/nucleon}$. The center thickness of the Al degrader is set to $44\,\%$ and $36.8\,\%$ of the ^{204}Au range for the Pb and U fragmentation reactions, respectively. This thickness combination of the production target and the degrader will ensure that the ^{204}Au ion has approximately $356\,\mathrm{MeV/nucleon}$ of kinetic energy after passing through the degrader. The Global calculations show that the proportion of fully stripped ^{204}Au ions at this energy is as high as $57\,\%$. Considering the proportion of fully stripped ions, the HFRS magnetic rigidity is set according to the fully stripped ones in both reactions.

Fig. 4 shows the simulated transmissions of the ^{204}Au fragment from the Pb and U fragmentation reactions as a function of the separator length. A significant decrease is observed near the PF1 and PF2. This is mainly caused by the momentum deviation. At the PF2 focal plane, the momentum slits are set to allow fragments with $\pm 0.2\,\%$ momentum deviation to pass through. In addition, the transmission of the ^{204}Au fragments produced by U fragmentation has a greater reduction due to the larger momentum deviation compared to the ones of Pb fragmentation. This is because in the U fragmentation reaction more nucleons need to be wiped out to produce ^{204}Au, which results in a greater momentum deviation of ^{204}Au fragments according to the Goldhaber model [61]. The opening of the mass slits placed at the PF4 focal plane can be adjusted based on the desired transmission and the number of nuclei required for mass measurements. In the simulation, the mass slits are set to $\pm 5\,\mathrm{mm}$. They also cause a decrease in the transmission due to the charge state population of fragments. At the final focal plane, the transmissions of ^{204}Au ions are $7\,\%$ and $2\,\%$ for Pb fragmentation and U fragmentation, respectively. These transmissions are significantly lower than the ones under the normal optical modes described in Ref. [31], mainly due to the smaller momentum and horizontal angular acceptances of the high resolution optical mode.

The yields and purities of ^{204}Au ions produced from the Pb and U fragmentation reaction are estimated and demonstrated in Fig. 5 (a) and (b), respectively. The area of the isotopes in the $N-Z$ plane represents the corresponding yields at the MF6 focal plane. The yields are obtained from the product of the production cross section, the number of target nucleons per unit area, and the transmission. The parametrized formula FRACS can provide a good description for the production cross section estimations [62]. For the number of target nucleons per unit area, it is calculated based on the thickness of the production target. The transmission is obtained from the MOCADI simulations. In addition, to assess the purity, nuclei located in the region of $Z \pm 10$ and $N \pm 10$ around ^{204}Au nucleus are selected in the simulation. The purity is defined as the ratio of the yield of the fragment of interest to the total. From Fig. 5, one can observe that for ^{204}Au ions, the Pb fragmentation reaction has a yield of up to $9.09 \times 10^4\,\mathrm{ppp}$ and a purity of about $3.69\,\%$. The yield and purity of ^{204}Au ions from the Pb fragmentation are higher than those of the U fragmentation reaction. Therefore, in future experiments, the Pb fragmentation reaction will be selected to produce ^{204}Au ions.

Using the calculated cross sections and the simulated transmissions, the yields of the neutron-rich nuclei around N=126 are estimated and shown in Fig. 6. In the estimations, the primary beam, the production target, and the settings of the HFRS are similar to the examples of production and purification for ^{204}Au ions. The production cross sections are calculated with the FRACS formula. Based on the aforementioned simulation results, the transmissions of fragments from Pb and U fragmentation reactions are fixed at $7\,\%$ and $2\,\%$, re-

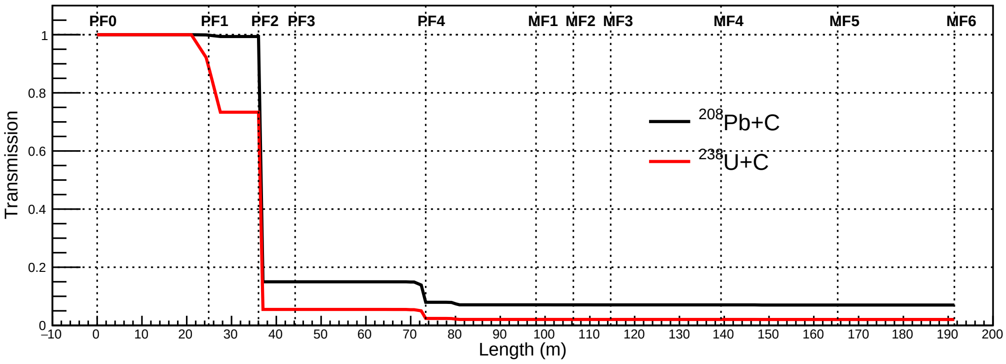

Fig. 4. (Color online) Simulated transmissions of the fragmentation product ^{204}Au as a function of the length of the HFRS separator under the high resolution mode.

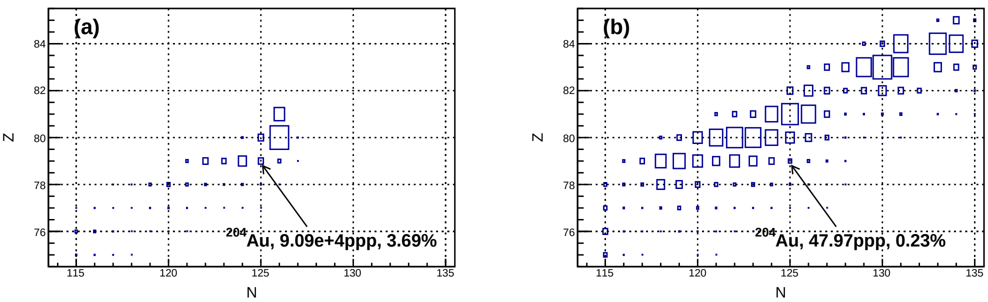

Fig. 5. (Color online) Purification quality of the HFRS for the ^{204}Au ions produced by (a) ^{208}Pb fragmentation and (b) ^{238}U fragmentation under high resolution optical mode.

spectively. The figure presents the results of a $5-$day experiment, showcasing the maximum yields of fragments of interest produced through the fragmentation reactions of Pb or U. It is obvious that many new neutron-rich nuclei approaching the r-process can be produced for the first time, alongside a substantial yield of neutron-rich nuclei with unknown mass and lifetime. This indicates that the HIAF-HFRS facility has great potential for the research on the production and properties of neutron-rich nuclei around N=126.

C. Identification and mass measurement

Taking the production of ^{204}Au ions by Pb fragmentation as an example, the particle identification and the accuracy of mass measurement using the $B\rho$-TOF method will be studied in this section.

As mentioned above, the particle identification will be achieved by the ΔE-TOF-$B\rho$ method. In the simulation, the influence of material thickness of TOF and position detectors on ion transmission and identification is ignored. This is because they have a thinner thickness compared to the range of the fragments of interest. The thickness of the MUSIC energy loss detector is equivalent to $300\,\mu\mathrm{m}$ thick Silicon. The time resolution (σ) of the TOF system is assumed to be $30\,\mathrm{ps}$. The position resolution (σ) of the position detector at the dispersive plane and the energy resolution (σ) of the ΔE detector are set to $0.5\,\mathrm{mm}$ and $0.4\,\%$, respectively. To obtain unambiguous particle identification, it is essential to correct the TOF values with the measured dispersive position information at the MF4 focal plane. This can remove the magnetic rigidity dependence from the measured TOF spectra. A two dimensional correlation between the TOF and the horizontal position x at the MF4 dispersion plane for Au isotopes is shown in Fig. 7 (a). For all nuclides, the deviation between their TOF and the central time-of-flight TOF_0 can be corrected using a linear function of the dispersive position x,

$$TOF_0 = TOF - kx. \tag{6}$$

Here k represents the slope of the fitted linear function. The corrected TOF vs. x spectrum is shown in Fig. 7 (b). The original and corrected TOF spectra for Au isotopes are compared in Fig. 7 (c). It is obvious that the corrected TOF has better resolution, which is beneficial for particle identification.

The two dimensional correlation spectrum of the measured ΔE and the corrected TOF can provide unambiguous particle identification, as shown in Fig. 8. By using the isomer tagging method, the cocktails can be unambiguously identified. In this experimental setting, the charge states between fully

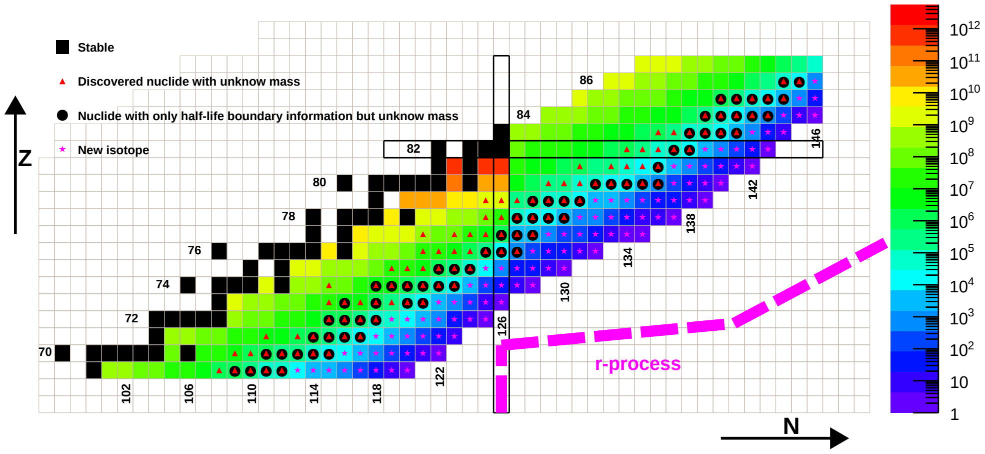

Fig. 6. (Color online) Estimated yields of the neutron-rich nuclei around N=126 using the FRACS formula and the simulated transmissions. The maximum fragment yields produced by the fragmentation of Pb or U with a $5-$day beam time are shown. The mass and lifetime information is extracted from NUBASE2020 [63].

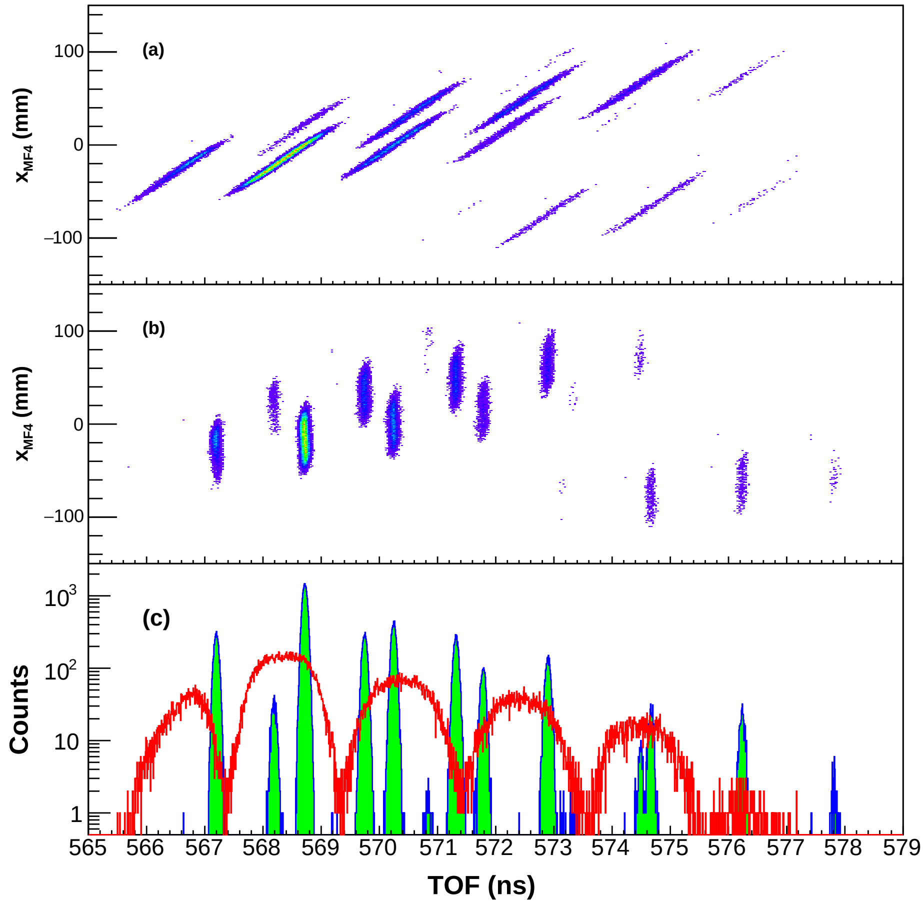

Fig. 7. (Color online) (a) Two dimensional correlation between the TOF and the horizontal position x of the dispersion plane for Au isotopes. (b) Corrected TOF vs. x spectrum. (c) Corrected TOF spectra (filled histograms) compared with raw ones (histograms with red lines).

stripped ions and helium-like ions are observed. As the fragments of interest are around $A = 2.58 \times Z$, the hydrogen-like

ions $^{A}Z^{(Z-1)+}$ general appear between the fully stripped ions with $^{A+2}Z^{Z+}$ and $^{A+3}Z^{Z+}$, and the helium-like ions $^{A}Z^{(Z-2)+}$ appear between the ions with $^{A+5}Z^{Z+}$ and $^{A+6}Z^{Z+}$ in the TOF spectra. This rule is helpful for particle identification. In addition, the degrader installed at the PF2 dispersive plane will change the charge state population of the fragments passing through it. The nuclides circled with red dash line remain unchanged in the charge state before and after the degrader. The nuclides that have been stripped of one electron by the degrader fall into the circle with black dash line. Under the same magnetic rigidity, these nuclides have higher velocities and shorter flight times. On the contrary, the nuclides that capture an electron from the degrader have lower velocities and longer flight times, as shown in the circle with green dash line in Fig. 8.

Using the obtained particle identification spectra, we will study the mass measurement precision of neutron-rich nuclei around N=126 using the $B\rho$-TOF method on the HFRS. The data analysis methodology is basically consistent with the Refs. [64, 65]. Typically, nuclei with known masses are used to calibrate the relationship between the time-of-flight and mass-to-charge ratios. This can help to remove a lot of uncertainties in the mass measurement experiment. Among the identified cocktails, ten fully stripped nuclides with well-known masses according to the 2012 Atomic Mass Evaluation (AME2012) [66] were selected as calibrants. In addition, these chosen nuclides only have known isomers with excitation energies below 454 keV, which corresponds to the typical mass accuracy using the $B\rho$-TOF technique. The calibrants and their atomic mass excess values with uncertainties are listed in the left columns of Table 1. The right columns of Table 1 list the nuclides to be measured and their mass excess values from the literature [66].

TABLE 1. Nuclides and their atomic mass excess values with uncertainties used for the calibration and measurement [66]. Isotopes with known isomers with excitation energies below 454 keV are shown with ^{m}, and isotopes with estimated atom mass excess are labeled with $^{\#}$.

Calibration nuclides			Nuclides to be measured		
Isotope	AME2012 (keV)	σ_m (keV)	Isotope	AME2012 (keV)	σ_m (keV)
^{194}Os	-32437.2	2.78	^{198}Ir$^{\#}$	-25821$^{\#}$	196$^{\#}$
^{195}Os^{m}	-29511.6	60.55	^{200}Ir$^{\#}$	-21611$^{\#}$	196$^{\#}$
^{196}Os	-28278.8	10.06	^{201}Ir$^{\#}$	-19897$^{\#}$	196$^{\#}$
^{196}Ir^{m}	-29437.9	38.42	^{202}Pt	-22692.1	25.15
^{197}Ir^{m}	-28265.8	20.12	^{203}Pt$^{\#}$	-19627$^{\#}$	196$^{\#}$
^{199}Ir	-24400.2	41.06	^{203}Au	-23143.5	3.08
^{199}Pt^{m}	-27390.4	2.22	^{204}Au$^{\#}$	-20650$^{\#}$	200$^{\#}$
^{200}Pt	-26600.9	20.12	^{205}Au$^{\#}$	-18770$^{\#}$	196$^{\#}$
^{201}Pt	-23740.9	50.1			
^{202}Au	-24353.0	23.29			

The nuclear masses m can be determined from the corresponding atomic masses ma utilizing the following formula,

$$m = m_a - Zm_e + B_e(Z), \tag{7}$$

where Z and m_e represent the nuclear charge number and electron rest mass, respectively. $B_e(Z)$ denotes the total binding energy of the extranuclear electrons. It is calculated with an approximate formula [67],

$$B_e(Z) = 14.438Z^{2.39} + 1.55468 \times 10^{-6} Z^{5.35} [eV]. \tag{8}$$

From the corrected TOF spectra, the Gaussian fitting function is employed to extract the centroids and standard deviations of the $TOFs$ for both calibration and measurement nuclides. Then we can get the mass calibration function $f(\tau, Z)$ according to the relationship between the time-of-flight centroids τ and the mass-to-charge ratios m/q with the following relation,

$$f(\tau, Z) = m/q = a_0 + a_1\tau + a_2\tau^2 + a_3\tau Z + a_4 Z + a_5 Z^2, \tag{9}$$

where a_i are fit parameters. The terms related to Z are necessary to account for the impact of the energy loss in the wedge degrader at the PF2 dispersive plane. The fit parameters in Eq. (9) are determined by an iterative χ^2 minimization procedure,

$$\chi^2 = \sum_{i=1}^{n} \frac{[(m/q)_{i,AME} - f(\tau_i, Z_i)]^2}{(\sigma_{AME})_i^2 + (\sigma_{stat})_i^2} \tag{10}$$

where n is the number of the calibrants, $(m/q)_{i,AME}$ is each calibration mass-to-charge ratio from AME2012 [66], $(\sigma_{AME})_i$ and $(\sigma_{stat})_i$ denote the uncertainty of the mass-to-charge ratio from the literature [66] and the statistical uncertainty, respectively. The statistical uncertainty is calculated based on the TOF measurement uncertainty,

$$(\sigma_{stat})_i^2 = \frac{\sigma_{i,TOF}^2}{N_i}(a_1 + 2a_2\tau + a_3 Z)^2, \tag{11}$$

where $\sigma_{i,TOF}$ is the standard deviations of the TOF distribution, and N_i is the statistical count for each calibration.

After obtaining the fit parameters, the masses of these measurement nuclides can be calculated from the corresponding time-of-flight centroids using Eq. (9). The total uncertainties in the mass results mainly include statistical uncertainties, fitting uncertainties, and systematic uncertainties. The statistical uncertainty can be estimated with Eq. (11). The fitting uncertainty σ_{fit} comes from the uncertainty of the calibration function parameters. It is calculated from the error propagation based on Eq. (9),

$$\sigma_{fit}^2 = \sum_{j=0}^{5}\sum_{i=0}^{5}[\sigma_{ij}^2 \frac{\partial f(\tau, Z)}{\partial a_j}\frac{\partial f(\tau, Z)}{\partial a_i}], \tag{12}$$

where σ_{ij} is the covariances of the fit parameters. The fit can be performed by the TMinuit class of the CERN root package [68], which provides an estimation for the covariance matrix. The systematic uncertainty σ_{sys} mainly comes from the velocity difference caused by the change in charge state in the wedge degrader and the method employed to correct TOF by dispersive position. We can use the method of cross validation of the calibration nuclides to evaluate the systematic errors. Assuming there are a total of n calibration

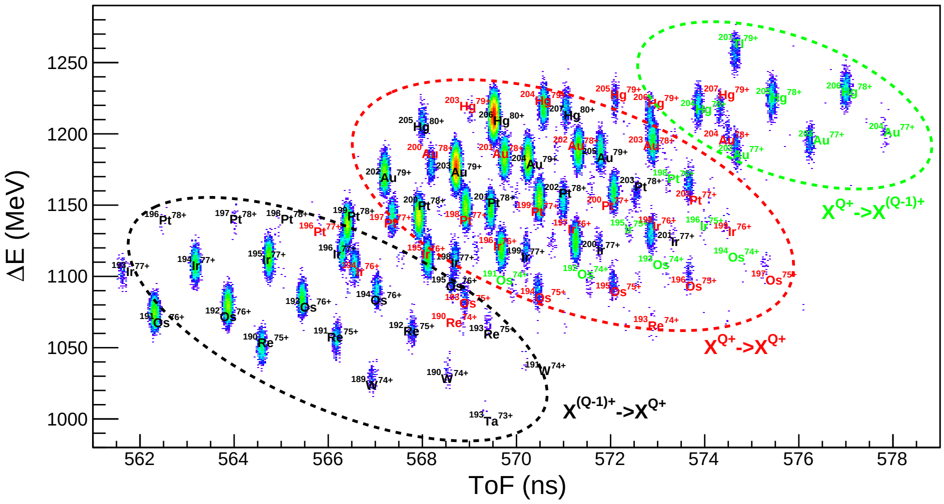

Fig. 8. (Color online) Two dimensional correlation spectrum of the measured ΔE and the corrected TOF. Fully stripped fragments, hydrogen-like fragments, and helium-like fragments are labeled with black fonts, red fonts, and green fonts, respectively. The black, red, and green circles indicate the isotopes stripped of one electron, the isotopes whose charge states unchanged, and the isotopes captured an electron at the PF2 degrader, respectively.

nuclides, we determine the m/q value for each of the nuclides by calibrating the fitting function of Eq. (9) with the remaining $n-1$ nuclides. Then the normalized chi-square value can be calculated as,

$$\chi^2_{norm} = \frac{1}{n}\sum_{i=1}^{n}\frac{[(m/q)_{i,AME} - (m/q)_{i,fit}]^2}{(\sigma_{AME})_i^2 + (\sigma_{stat})_i^2 + (\sigma_{fit})_i^2 + \sigma_{sys}^2}, \tag{13}$$

The differences between the masses from the literature [66] and values given by the fitting function as a function of the mass-to-charge ratio are shown in Fig. 9 for the calibration nuclides (circles) and measured nuclides (squares), and the atomic mass excess results and the different contributions to the total uncertainties for both the calibration and measured nuclides are listed in Table 2. For the statistical uncertainties, they are estimated using $5-$day statistical counts with Eq. (11). The ^{201}Ir, ^{203}Pt, and ^{205}Au nuclei in Table 2 have significant fitting uncertainties. This is because these nuclei have larger mass-to-charge ratios than the calibration nuclides, and their masses were extrapolated. If more calibration nuclides can be selected to cover the mass-to-charge ratios of the measured nucleus, smaller fitting uncertainties can be obtained. The systematic uncertainty is determined as $7.73\,\mathrm{keV/q}$ to achieve a normalized chi-square value of unity in Eq. (13). From Table 2, the total measurement uncertainties mainly come from the system uncertainties. This is mainly caused by the TOF correction. Using more measurement information, such as position and angle information at the PF4 or MF6, may reduce the system uncertainties. The total measurement uncertainty of the measured nuclei is better than $900\,\mathrm{keV}$. This measurement accuracy can meet the requirements of some physical research, proving that the properties of some neutron-rich nuclei near N=126 can be studied based on the HFRS separator.

TABLE 2. Nuclides and their atomic mass excess values with uncertainties obtained from the mass calibration function. Different contributions to the total uncertainties are shown. Isotopes with estimated atom mass excess in the literature [66] are labeled with $^{\#}$.

Isotope	m_{fit} (keV)	σ_{total} (keV)	Uncertainties		
			σ_{stat} (keV)	σ_{fit} (keV)	σ_{sys} (keV)
^{194}Os	-33701.6	606.26	106.78	104.37	587.59
^{195}Os^m	-28961.5	593.94	77.02	39.7	587.59
^{196}Os	-28447.8	595.61	91.99	32.14	587.59
^{196}Ir^m	-29637.7	598.31	26.19	53.73	595.32
^{197}Ir^m	-28296.1	595.85	22.64	10.88	595.32
^{199}Ir	-24435.8	596.86	41.33	11.57	595.32
^{199}Pt^m	-27171.2	603.37	12.0	15.49	603.05
^{200}Pt	-26692.6	603.15	8.94	6.25	603.05
^{201}Pt	-23709.1	603.23	12.98	6.77	603.05
^{202}Au	-24438.1	611.98	7.84	37.54	610.78
^{198}Ir$^{\#}$	-26374.9	596.01	28.11	11.87	595.32
^{200}Ir$^{\#}$	-21921.2	611.06	61.41	123.38	595.32
^{201}Ir$^{\#}$	-18796.2	868.45	118.62	621.08	595.32
^{202}Pt	-22580.8	608.4	19.88	78.02	603.05
^{203}Pt$^{\#}$	-18348.8	743.61	35.16	433.65	603.05
^{203}Au	-22687.2	613.34	3.65	55.82	610.78
^{204}Au$^{\#}$	-19643.5	635.88	5.96	176.81	610.78
^{205}Au$^{\#}$	-16541.0	827.99	10.64	558.92	610.78

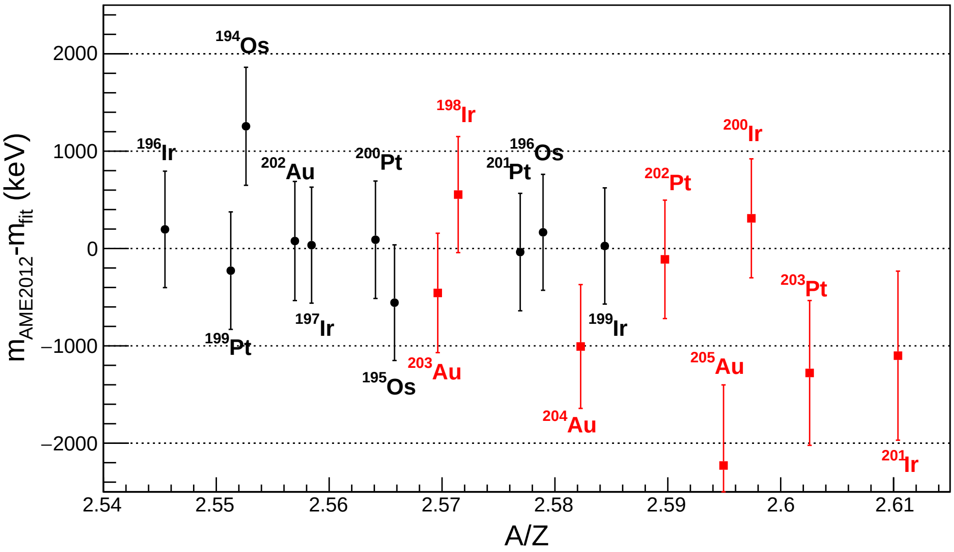

Fig. 9. (Color online) Differences between the fit masses and the values from AME2012 as a function of the mass-to-charge ratio. The circles and squares represent the results of the calibration and measured nuclides, respectively. The error bars of the calibration nuclides include the literature uncertainty and the total measurement uncertainty. The uncertainty of the measured nuclides is only the total measurement uncertainty.

IV. SUMMARY

The properties of N=126 neutron-rich nuclei play crucial roles in developing nuclear theories and understanding the r-process abundance peak around A=195. To produce these neutron-rich nuclei while measuring their mass and lifetime, an experimental scheme has been proposed based on the HIAF-HFRS facility, and the feasibility of this scheme was also evaluated by the simulations in this paper.

For these studies, a high resolution optical mode of the HFRS was specially developed. It has a large momentum dispersion of $12\,\mathrm{cm}/\%$ at the MF4 dispersive plane, which is beneficial for improving the accuracy of magnetic rigidity measurement in $B\rho$-TOF mass measurement experiments. Under this high resolution optical mode, the yields of the neutron-rich nuclei around N=126 produced from ^{208}Pb or ^{238}U fragmentation reactions were estimated using the FRACS formula and the simulated transmissions. The results show that many new neutron-rich nuclei approaching the r-process abundance peak around A=195 can be produced for the first time, and many nuclei with unknown mass and lifetime can be produced with high statistics. Moreover, using the time-of-flight corrected by the measured dispersive position information and the energy loss information, the cocktails produced from the ^{208}Pb fragmentation can be unambiguously identified, and the masses of some neutron-rich nuclei around N=126 can be measured with an accuracy better than $900\,\mathrm{keV}$ by using the $B\rho$-TOF technique. Using these new mass data, combined with the machine learning based on the Bayesian neural network as described in Refs. [7, 8], the nuclear mass of this region will be further accurately predicted, which is crucial for understanding the r-process abundance peak around A=195. These simulation results indicate that the HIAF-HFRS facility can provide an opportunity for production and property research of neutron-rich nuclei around N=126.

At present, the HIAF-HFRS facility is under construction. All devices including magnets, vacuum, power supply, targets, degraders, detectors, etc. are expected to be completed and tested by the end of 2024, after which they can be installed on-site. Meanwhile, some high performance detectors for the TOF and position measurements used in $B\rho$-TOF mass measurement experiments have been proposed. For example, the plastic scintillator detector coupled with multiple photomultiplier tube readouts and the diamond detector are being developed for time measurements, and the position-sensitive micro-channel-plate detector with a large active area is also being developed for position measurements. These conditions may ensure the carry out of future property research experiments of neutron-rich nuclei around N=126.

V. ACKNOWLEDGMENTS

This work was supported by High Intensity heavy-ion Accelerator Facility (HIAF) project approved by the National Development and Reform Commission of China.

[1] T. Kajino, Underground laboratory JUNA shedding light on stellar nucleosynthesis. Nucl. Sci. Tech. **34**, 42 (2023). doi:10.1007/s41365-023-01196-1

[2] B. Guo, W. P. Liu, X. D. Tang et al., Research program of nuclear astrophysics based on the HIAF. SCIENTIA SINICA Physica, Mechanica & Astronomica **50**, 112007 (2020). doi:10.1360/SSPMA-2020-0281

[3] Y. G. Ma, Annual review of the advances in nuclear physics. Science & Technology Review **41**, 14 (2022). doi:10.3981/j.issn.1000-7857.2023.01.002

[4] Y. F. Gao, B. S. Cai, C. X. Yuan, Investigation of β^- decay half-life and delayed neutron emission with uncertainty analysis. Nucl. Sci. Tech. **34**, 9 (2023). doi:10.1007/s41365-022-01153-4

[5] M. Shi, J. Y. Fang, Z. M. Niu, Exploring the uncertainties in theoretical predictions of nuclear β-decay half-lives. Chinese Physics C **45**, 044103 (2021). doi:10.1088/1674-1137/abdf42

[6] Z. Chen, X. P. Zhang, H. Y. Yang et al., β^--decay half-lives for waiting point nucleiaround N=82. Acta Phys. Sin. **63**, 162301 (2014). doi:10.7498/aps.63.162301

[7] Z. M. Niu, H. Z. Liang, B. H. Sun et al., Predictions of nuclear β-decay half-lives with machine learning and their impact on r-process nucleosynthesis. Physical Review C **99**, 064307 (2019). doi: 10.1103/PhysRevC.99.064307

[8] Z. M. Niu, H. Z. Liang, Nuclear mass predictions with machine learning reaching the accuracy required by r-process studies. Physical Review C **106**, L021303 (2022). doi:10.1103/PhysRevC.106.L021303

[9] X. F. Jiang, X. H. Wu, P. W. Zhao, Sensitivity Study of r-process Abundances to Nuclear Masses. The Astrophysical Journal **915**, 29 (2021). doi: 10.3847/1538-4357/ac042f

[10] Z. Li, Z. M. Niu, B. H. Sun, Influence of nuclear physics inputs and astrophysical conditions on r-process. SCIENCE CHINA Physics, Mechanics & Astronomy **62**, 982011 (2019). doi:10.1007/s11433-018-9355-y

[11] F. Niu, P. H. Chen, H. G. Cheng et al., Multinucleon transfer dynamics in nearly symmetric nuclear reactions. Nucl. Sci. Tech. **31**, 59 (2020). doi:10.1007/s41365-020-00770-1

[12] X. Jiang, N. Wang, Production mechanism of neutron-rich nuclei around N=126 in the multi-nucleon transfer reaction ^{132}Sn+^{208}Pb. Chinese Physics C **42**, 104105 (2018). doi:10.1088/1674-1137/42/10/104105

[13] P. H. Chen, C. Geng, Z. X. Yang et al., Production of neutron-rich actinide isotopes in isobaric collisions via multinucleon transfer reactions. Nucl. Sci. Tech. **34**, 160 (2023). doi:10.1007/s41365-023-01314-z

[14] Z. H. Liao, L. Zhu, Z. P. Gao et al., Optimal detection angles for producing N=126 neutron-rich isotones in multinucleon transfer reactions. Phyiscal Review Research **5**, L022021 (2023). doi:10.1103/PhysRevResearch.5.L022021

[15] Y. Hirayama, Y.X. Watanabe, M. Mukai et al., Doughnut-shaped gas cell for KEK Isotope Separation System. Nucl. Instrum. Methods. Phys. Res. B **412**, 11 (2017). doi:10.1016/j.nimb.2017.08.037

[16] A. Spătaru, D.L. Balabanski, O. Beliuskina et al., Production of Exotic Nuclei via MNT Reactions Using Gas Cells. Acta Phys. Pol. B **51**, 817 (2020). doi:10.5506/APhysPolB.51.817

[17] G. Savard, M. Brodeur, J. A. Clark et al., The N=126 factory: A new facility to produce very heavy neutron-rich isotope. Nucl. Instrum. Methods. Phys. Res. B **463**, 258 (2020). doi:10.1016/j.nimb.2019.05.024

[18] A. Rotaru, D. Amanbayev, D. L. Balabanski et al., SINCREASE: An in-cell reaction system for multi-nucleon transfer and spontaneous fission at the FRS ion catcher. Nucl. Instrum. Methods. Phys. Res. B **512**, 83 (2022). doi:10.1016/j.nimb.2021.11.018

[19] M. Mukai, Y. Hirayama, Y. X. Watanabe et al., In-gas-cell laser resonance ionization spectroscopy of ^{196,197,198}Ir. Rhys. Rev. C **102**, 054307 (2020). doi:10.1103/PhysRevC.102.054307

[20] H. Choi, Y. Hirayama, S. Choi et al., In-gas-cell laser ionization spectroscopy of ^{194,196}Os isotopes by using a multireflection time-of-flight mass spectrograph. Rhys. Rev. C **102**, 034309 (2020). doi:10.1103/PhysRevC.102.034309

[21] M. Huyse, M. Facina, Y. Kudryavtsev et al., Intensity limitations of a gas cell for stopping, storing and guiding of radioactive ions. Nucl. Instrum. Methods. Phys. Res. B **187**, 535 (2002). doi: 10.1016/S0168-583X(01)01152-1

[22] Y. S. Wang, W. X. Huang, Y. L. Tian et al., Monte-Carlo simulation of ion distributions in a gas cell for multinucleon transfer reaction products at LENSHIAF spectrometer. Nucl. Instrum. Methods. Phys. Res. B **463**, 528 (2020). doi:10.1016/j.nimb.2019.02.013

[23] J. Even, X. Chen, A. Soylu et al., The NEXT Project: Towards Production and Investigation of Neutron-Rich Heavy Nuclides. Atoms **10(2)**, 59 (2022). doi:10.3390/atoms10020059

[24] T. Aoki, Y. Hirayama, H. Ishiyama et al., Design report of the KISS-II facility for exploring the origin of uranium. arXiv: **2209**, 12649[physics.ins-det] (2022). doi:10.48550/arXiv.2209.12649

[25] J. Kurcewicz, F. Farinon, H. Geissel et al., Discovery and cross-section measurement of neutron-rich isotopes in the element range from neodymium to platinum with the FRS. Phys. Lett. B **717**, 371 (2012). doi:10.1016/j.physletb.2012.09.021

[26] T. Kurtukian-Nieto, J. Benlliure, K.-H. Schmidt et al., Production cross sections of heavy neutron-rich nuclei approaching the nucleosynthesis r-process path around A=195. Phys. Rev. C **89**, 024616 (2014). doi:10.1103/PhysRevC.89.024616

[27] C. W. Ma, H. L. Wei, X. Q. Liu et al., Nuclear fragments in projectile fragmentation reactions. Prog. Part. Nucl. Phys. **121**, 103911 (2021). doi:10.1016/j.ppnp.2021.103911

[28] J. S. Winfield, H. Geissel, B. Franczak et al., Ion-optical developments tailored for experiments with the Super-FRS at FAIR. Nucl. Instrum. Methods. Phys. Res. B **491**, 38 (2021). doi:10.1016/j.nimb.2021.01.004

[29] W. R. Plaß, T. Dickel, I. Mardor et al., The science case of the FRS Ion Catcher for FAIR Phase-0. Hyperfine Interact **240**, 73 (2019). doi:10.1007/s10751-019-1597-4

[30] L. N. Sheng, X. H. Zhang, J. Q. Zhang et al., Ion-optical design of High energy FRagment Separator (HFRS) at HIAF. Nucl. Instrum. Methods. Phys. Res. B **469**, 1 (2020). doi:10.1016/j.nimb.2020.02.026

[31] L. N. Sheng, X. H. Zhang, H. Ren et al., Ion-optical updates and performance analysis of High energy FRagment Separator (HFRS) at HIAF. Nucl. Instrum. Methods. Phys. Res. B **547**, 165214 (2024). doi:10.1016/j.nimb.2023.165214

[32] J. C. Yang, J. W. Xia, G. Q. Xiao et al., High Intensity heavy ion Accelerator Facility (HIAF) in China. Nucl. Instrum. Methods. Phys. Res. B **317**, 263 (2013). doi:10.1016/j.nimb.2013.08.046

[33] Y. Yang, Y. W. Su, W. Y. Li et al., Evaluation of radiation environment in the target area of fragment separator HFRS at HIAF. Nucl. Sci. Tech. **29**, 147 (2018). doi:10.1007/s41365-018-0479-9

[34] K.-H. Schmidt, E. Hanelt, H. Geissel et al., The momentum-loss achromat — A new method for the isotopical separation of relativistic heavy ions. Nucl. Instrum. Methods. Phys. Res. A **260**, 287 (1987). doi:10.1016/0168-9002(87)90092-1

[35] B. H. Sun, J. W. Zhao, X. H. Zhang et al., Towards the full realization of the RIBLL2 beam line at the HIRFL-CSR complex. Science Bulletin **63**, 78 (2018). doi:10.1016/j.scib.2017.12.005

[36] W. Liu, J. L. Lou, Y. L. Ye et al., Experimental study of intruder components in light neutron-rich nuclei via single-nucleon transfer reaction. Nucl. Sci. Tech. **31**, 20 (2020). doi:10.1007/s41365-020-0731-y

[37] J. Chen, J. L. Lou, Y. L. Ye et al., A new measurement of the intruder configuration in ^{12}Be. Physics Letters B **781**, 412 (2018). doi:10.1016/j.physletb.2018.04.016

[38] W. Q. Zhang, A. N. Andreyev, Z. Liu et al., First observation of a shape isomer and a low-lying strongly-coupled prolate band in neutron-deficient semi-magic ^{187}Pb. Physics Letters B **829**, 137129 (2022). doi:10.1016/j.physletb.2022.137129

[39] X. H. Zhang, S. W. Tang, P. Ma et al., A multiple sampling ionization chamber for the External Target Facility. Nucl. Instrum. Methods. Phys. Res. A **795**, 389 (2015). doi:10.1016/j.nima.2015.06.022

[40] S. W. Tang, L. M. Duan, Z. Y. Sun et al., A Longitudinal Field Multiple Sampling Ionization Chamber for RIBLL2. Nuclear Physics Review **29**, 72 (2012). doi:10.11804/NuclPhysRev.29.01.072

[41] J. H. Liu, Z. Ge, Q. Wang et al., Electrostatic-lenses position-sensitive TOF MCP detector for beam diagnostics and new scheme for mass measurements at HIAF. Nucl. Sci. Tech. **30**, 152 (2019). doi:10.1007/s41365-019-0676-1

[42] A. Gillibert, L. Bianchi, A. Cunsolo et al., Mass measurement of light neutron-rich fragmentation products. Phys. Lett. B **176**, 317 (1986). doi:10.1016/0370-2693(86)90171-1

[43] B. H. Sun, J. W. Zhao, W. Q. Yan et al., A new Time-of-Flight mass measurement project for exotic nuclei and ultra-high precision detector development. EPJ Web of Conferences **109**, 04008 (2016). doi:10.1051/epjconf/201610904008

[44] F. Fang, S. Tang, S. Wang et al., Improving the Particle Identification of Radioactive Isotope Beams at the RIBLL2 Separator. Nuclear Physics Review **39**, 65 (2022). doi:10.11804/NuclPhysRev.39.2021035

[45] Z. Meisel, S. George, S. Ahn et al., Mass Measurements Demonstrate a Strong N=28 Shell Gap in Argon. Phys. Rev. Lett. **114**, 022501 (2015). doi:10.1103/PhysRevLett.114.022501

[46] Z. Meisel, S. George, S. Ahn et al., Mass Measurement of ^{56}Sc Reveals a Small A=56 Odd-Even Mass Staggering, Implying a Cooler Accreted Neutron Star Crust. Phys. Rev. Lett. **115**, 162501 (2015). doi:10.1103/PhysRevLett.115.162501

[47] S. Michimasa, M. Kobayashi, Y. Kiyokawa et al., Magic Nature of Neutrons in ^{54}Ca: First Mass Measurements of $^{55-57}$Ca. Phys. Rev. Lett. **121**, 022506 (2018). doi:10.1103/PhysRevLett.121.022506

[48] S. Michimasa, M. Kobayashi, Y. Kiyokawa et al., Mapping of a New Deformation Region around ^{62}Ti. Phys. Rev. Lett. **125**, 122501 (2020). doi:10.1103/PhysRevLett.125.122501

[49] A.M. Rogers, A. Sanetullaev, W.G. Lynch et al., Tracking rare-isotope beams with microchannel plates. Nucl. Instrum. Methods. Phys. Res. A **795**, 325 (2015). doi:10.1016/j.nima.2015.05.070

[50] H. Kumagai, A. Ozawa, N. Fukuda et al., Delay-line PPAC for high-energy light ions. Nucl. Instrum. Methods. Phys. Res. A **470**, 562 (2001). doi:10.1016/S0168-9002(01)00804-X

[51] C. Scheidenberger, T. Stöhlker, W. E. Meyerhof et al., Charge states of relativistic heavy ions in matter. Nucl. Instrum. Methods. Phys. Res. B **142**, 441 (1998). doi:10.1016/S0168-583X(98)00244-4

[52] Z. Meisel, S. George, S. Ahn et al.,Time-of-flight mass measurements of neutron-rich chromium isotopes up to N=40 and implications for the accreted neutron star crust. Phys. Rev. C **93**, 035805 (2016). doi:10.1103/PhysRevC.93.035805

[53] K. Wang, A. Estrade, S. Neupane et al., Plastic scintillation detectors for time-of-flight mass measurements. Nucl. Instrum. Methods. Phys. Res. A **974**, 164199 (2020). doi:10.1016/j.nima.2020.164199

[54] S. Michimasa, M. Takaki, M. Dozono et al., Development of CVD diamond detector for time-of-flight measurements. Nucl. Instrum. Methods. Phys. Res. B **317**, 710 (2013). doi:10.1016/j.nimb.2013.08.055

[55] D. Lunney, J. M. Pearson, C. Thibault et al., Recent trends in the determination of nuclear masses. Rev. Mod. Phys. **75**, 1021 (2003). doi:10.1103/RevModPhys.75.1021

[56] A.K. Mistry, H.M. Albers, T. Arıcı et al., The DESPEC setup for GSI and FAIR. Nucl. Instrum. Methods. Phys. Res. B **1033**, 166662 (2022). doi:10.1016/j.nima.2022.166662

[57] S. Nishimura, Beta-gamma spectroscopy at RIBF. Prog. Theor. Exp. Phys. **2012**, 03C006 (2012). doi:10.1093/ptep/pts078

[58] N. Iwasa, H. Geissel, G. Münzenberg et al., MOCADI, a universal Monte Carlo code for the transport of heavy ions through matter within ion-optical systems. Nucl. Instrum. Methods. Phys. Res. B **126**, 284 (1997). doi:10.1016/S0168-583X(97)01097-5

[59] P. J. Bryant, AGILE, A Tool for Interactive Lattice Design. Proc. of EPAC. **2000**, 1357 (2000).

[60] H. Wollnik, B. Hartmann, M. Berz et al., Principles of GIOS and COSY. AIP Conf. Proc. **177**, 74 (1988). doi:10.1063/1.37817

[61] A. S. Goldhaber,Statistical models of fragmentation processes. Phys. Lett. B **53**, 306 (1974). doi:10.1016/0370-2693(74)90388-8

[62] B. Mei, Improved empirical parameterization for projectile fragmentation cross sections. Phys. Rev. C **95**, 034608 (2017). doi:10.1103/PhysRevC.86.014601

[63] F.G. Kondev, M. Wang, W.J. Huang et al., The NUBASE2020 evaluation of nuclear physics properties. Chinese Physics C **45**, 030001 (2021). doi:10.1088/1674-1137/abddae

[64] Z. Ge, Q. Wang, M. Wang et al., Study of Mass-measurement Method for N=Z Nuclei with Isochronous Mass Spectrometry. Nuclear Physics Review **36**, 294 (2019). doi: 10.11804/NuclPhysRev.36.03.294

[65] X. Xu, M. Wang, Y. H. Zhang et al., Direct mass measurements of neutron-rich ^{86}Kr projectile fragments and the persistence of neutron magic number N=32 in Sc isotopes. Chinese Physics C **39**, 104001 (2015). doi:10.1088/1674-1137/39/10/104001

[66] G. Audi, M. Wang, A. H. Wapstra et al., The Ame2012 atomic mass evaluation. Chinese Physics C **36**, 1287 (2012). doi:10.1088/1674-1137/36/12/002

[67] D. Lunney, J. M. Pearson, C. Thibault et al., Recent trends in the determination of nuclear masses. Review of Modern Physics **75**, 1021 (2003). doi:10.1103/RevModPhys.75.1021

[68] ROOT: analyzing petabytes of data, scientifically.